Computation of turbulent flow and secondary motions in a square duct using a forced generalized lattice Boltzmann equation

Martin J. Pattison*
MetaHeuristics LLC, 3944 State Street, Suite 350, Santa Barbara, California 93105, USA

Kannan N. Premnath†
Department of Chemical Engineering, University of California, Santa Barbara, California 93106, USA and MetaHeuristics LLC, 3944 State Street, Suite 350, Santa Barbara, California 93105, USA

Sanjoy Banerjee‡
Department of Chemical Engineering, Department of Mechanical Engineering, Bren School of Environmental Science and Management, University of California, Santa Barbara, California 93106, USA

(Received 26 April 2008; published 10 February 2009)

Turbulent flow in a straight square duct driven by a pressure gradient exhibits remarkable flow structures such as the presence of mean streamwise vorticity or secondary flows. These secondary circulations take the form of two counter-rotating vortices near each corner of the duct. Even though their magnitudes are small compared with primary streamwise motions, they have a significant influence on flow and scalar transport and are challenging to accurately predict using computational approaches. In this paper, we employ a recently developed formulation of the generalized lattice Boltzmann equation (GLBE) with forcing term to perform large eddy simulation of fully developed turbulent flow in a square duct at a shear Reynolds number based on duct width equal to 300. Subgrid scale effects are represented by the Smagorinsky eddy viscosity model, which is modified by the van Driest damping function in the near-wall regions, in this GLBE approach, which is based on multiple relaxation times. It was found that the GLBE is able to correctly reproduce the existence of mean secondary motions and the computed detailed structure of first- and second-order statistics of main and secondary motions are in good agreement with prior direct numerical simulations based on the solution of the Navier-Stokes equations and experimental data.

DOI: 10.1103/PhysRevE.79.026704 PACS number(s): 47.11.−j, 05.20.Dd, 47.27.E−

I. INTRODUCTION

Turbulent flow in noncircular straight ducts is characterized by the presence of mean cross-stream fluid motions. The presence of such striking mean secondary vortical structures in this class of turbulent flows has attracted much attention over the years, not only due to an interest in the fundamental understanding of their complex physical origins, but also because of their impact on flow and scalar transport in practical situations. A classic example of mean streamwise vorticity or secondary flows is that due to turbulent flow in a square duct, which was observed in measurements by Nikuradse in the 1920s [1]. Prandtl systematized various types of secondary flows based on their origins into two basic categories and recognized the role of turbulent fluctuations in generating secondary motions in noncircular conduits [2,3], which are often classified as Prandtl's *secondary flows of the second kind*. On the other hand, for completeness, it may be noted that the *secondary flows of the first kind* in Prandtl's classification arise as quasi-inviscid skewed motions due to transverse pressure gradients, or Coriolis or other inertial forces [4].

Statistically averaged turbulence-induced secondary flows in a square duct manifest themselves with eightfold symmetry. That is, the mean velocity field consist of two counter-rotating vortices distributed in pairs in the four quadrants of the duct and advect fluid momentum from the bulk region to the corner areas of the duct along each corner bisector, which is transported back to the bulk regions along wall bisectors. The general features are not overly sensitive to the Reynolds number, except that it should be high enough that the flow is fully turbulent. On the other hand, interestingly, a recent study has shown that if the Reynolds number is such that the flow is only marginally turbulent, the secondary flow structure exhibits in the form of four vortices alternating in time, instead of the eight vortices in the case fully developed turbulent flow [5]. It may be noted that although the magnitude of secondary velocities is generally small, of the order of 1%–3% of the mean streamwise velocity, they can contribute considerably to the wall stress distribution and transport of momentum, vorticity, energy, and passive scalars [6].

The mechanism responsible for these secondary circulations has been a subject of long-standing debate. Brundrett and Baines [7] provided an explanation in terms of gradient in Reynolds stress as a source that give rise to mean streamwise vorticity. Gessner [8] provided a more proper description of the origin of secondary flows in terms of the inhomogeneity and anisotropy of Reynolds stress, although the role played by each of its components was not fully understood. More recently, direct numerical simulations (DNS) of turbulent flow in a square duct by Gavrilakis [9] and Huser and Biringen [10] yielded quantitative description of the structure

*martin@metah.com
†nandha@metah.com
‡banerjee@engineering.ucsb.edu

of secondary motions and fundamental insights into their origins. In particular, DNS of Gavrilakis [9] provided detailed turbulence statistics of primary and secondary motions along various wall and corner bisectors in the duct, while a quadrant analysis of Huser and Biringen [10] provided mechanisms for generation of secondary flows in terms of bursting and ejection events.

Turbulence modeling for computation of secondary flows generated by turbulent fluctuations has been very challenging and difficulties are faced with using common Reynolds-averaged turbulence models. Some of the early modeling efforts along with work on experimental measurements for this problem were reviewed in Ref. [11]. For example, the well-known and popular standard k-ϵ model was unable to predict any secondary flow. In a seminal analytical work, Speziale [12] found that secondary flows in noncircular ducts result from a nonzero difference in the normal stresses in the transverse plane. With the use of nonlinear forms of the k-ϵ equations that accounts for the delicate anisotropy in the normal components of the Reynolds stress [13,14], or by using more involved transport equations for Reynolds stress, it was possible to capture the existence of secondary flows. However, comparisons between computed results and experimental measurements were not entirely satisfactory, which is probably due to the need provide *a priori* modeling information from empirical correlations. Thus, in general, the presence of considerable empiricism built into the Reynolds-averaged turbulence modeling approaches substantially reduces their predictive capabilities for this problem.

On the other hand, secondary flows actually evolve from the collective behavior of individual realization of time-dependent turbulence fields. Direct numerical simulation resolves all spatial and temporal scales and can thus predict all possible motions and structural features due to turbulence with high fidelity. On the other hand, the computational cost of DNS limits its utility to low Reynolds numbers. In view of this, it is often more practical to use large eddy simulation (LES), where fluid motions with length scales greater than the grid size are computed and the effect of the unresolved eddies at subgrid scales (SGS) are modeled. As such, large scales represent the anisotropic part of the energy spectrum and contain most of the energy of the fluid motions. The smaller SGS scales are generally considered to be isotropic in nature and relatively independent of the resolved part of the spectrum. Thus LES represents a compromise with reduced empiricism in contrast to Reynolds-averaged models, but with reduced computational cost in comparison with DNS. Indeed, LES with using filtered Navier-Stokes equations (NSE) and Smagorinsky eddy viscosity model for SGS effects [15] by Madabhushi and Vanka [16] has yielded quantitative description of the structure of secondary motions in a turbulent square duct.

In the present work, we employ an alternative computational method based on the lattice Boltzmann method (LBM) to perform LES of turbulent flow and secondary motions in a square duct. The LBM, which is based on kinetic theory, is a relatively recent approach for computational fluid dynamics and other problems [17,18]. It involves solving a kinetic equation, the lattice Boltzmann equation (LBE), which represents the propagation of particle populations and their collisions along discrete directions on a lattice. The long term spatial and temporal dynamics of the LBE asymptotically corresponds to the fluid flow described by the weakly compressible Navier-Stokes equations when the lattice is constructed to respect sufficient rotational symmetries. The attractiveness of LBM comes from its simplicity of the stream-and-collide computational procedure, ability to represent boundary conditions in complex geometries, natural amenability for implementation on parallel computers with near-linear scalability, and its ability to more naturally model complex physics derived from kinetic theory. As a result, it has found a wide variety of applications, see, e.g., Refs. [19,20].

A commonly used form of the LBM employs a single relaxation time (SRT) model [21] to represent the effect of particle collisions, in which particle distributions relax to their local equilibrium at a rate determined by a single parameter [22,23]. On the other hand, an equivalent representation of distribution functions is in terms of their moments, such as various hydrodynamic fields including density, mass flux, and stress tensor. The relaxation process due to collisions can more naturally be described in terms of a space spanned by such moments, which can, in general relax at different rates. This forms the basis of the generalized lattice Boltzmann equation (GLBE) based on multiple relaxation times (MRT) [24–26]. By carefully separating the time scales of various hydrodynamic and kinetic modes through a linear stability analysis, the numerical stability of the GLBE or MRT LBE can be significantly improved when compared with the SRT LBE, particularly for more demanding problems at high Reynolds numbers [25]. The MRT LBE has also been extended for multiphase flows with superior stability characteristics [27–29], and, more recently, for magnetohydrodynamic problems [30]. It has also been used for LES of a class of turbulent flows [31,32].

In particular, recently, Yu *et al.* [32] pioneered the development of a robust approach based on MRT LBE for LES using the three-dimensional nineteen velocity (D3Q19) model. They employed a constant Smagorinsky model in which the SGS Reynolds stress is computed based on the local strain rate tensor. They related the strain rate tensor to the nonequilibrium part of the moments and validated their approach for turbulent free-shear flows. More recently, Premnath *et al.* [33] developed an LES framework, which is an extension of Yu *et al.* [32] for wall-bounded turbulent flows, which are driven or modulated by external forces. In particular, they considered the GLBE augmented by a forcing term, which is executed in its natural moment space. Such forcing term can represent the effect of general nonuniform forces on the turbulent fluid motion. Subgrid scale effects were represented by the Smagorinsky eddy viscosity model, which is modified by the van Driest wall damping function to account for reduction of near-wall turbulent length scales in wall-bounded flows. The strain rate tensor in this formulation is again related to the nonequilibrium moments with additional contributions from moment projections of forcing terms. They validated this framework for two canonical wall-bounded flows.

Unlike well established classical computational methods, such as spectral or finite difference methods, which have been thoroughly assessed for different complex turbulent flows during the last few decades, much remains unknown regarding computational approaches such as the LBM for such flows. Thus, there is a great need for studying and assessing LBM for complex turbulent flows in different configurations. Indeed, in recent years, there have been considerable efforts in this area, as briefly discussed in Ref. [33]. Several independent studies based on the LBM have been performed, each dealing with different configurations and conditions, and much of such prior efforts have focused on canonical problems in which turbulent flows are generally isotropic and homogeneous. Among these efforts, Yu *et al.* [32] employed their approach for LES of free-shear flow consisting of a jet issued from a square orifice issued in free space. On the other hand, the character of turbulent motion is dramatically different in the presence of either stationary or moving boundaries, which makes their statistical features to be more anisotropic and inhomogeneous. Thus, Premnath *et al.* [33] studied and assessed the MRT LBE with forcing term for LES of turbulent channel flow and turbulent flow in a cavity.

On the other hand, simulation of the detailed structure of turbulence-induced secondary fluid motion in noncircular conduits such as square ducts presents a particularly significant challenge to the computational methods, since as mentioned above, their magnitudes are relatively small and arise from turbulence anisotropy resulting from a delicate balance of Reynolds stresses. Few detailed LES studies for turbulent flow in a square duct. In particular, Madabhushi and Vanka [16] employed a finite-difference approach for LES on a relatively coarse grid and their results were found to be in qualitative agreement with dated experiments. On the other hand, Gavrilakis [9] and Cheesewright *et al.* [34] respectively provide high resolution DNS and experimental data for the detailed structure of first- and second-order statistics of main and secondary fluid motions at various locations in the duct. It is highly desirable to perform LES that make direct comparison with such reliable high resolution data. In particular, to the best of our knowledge, such a study is lacking using the LBM.

Thus, one of the objectives of this present work is perform a systematic study of LES using MRT LBE or GLBE with forcing term for turbulent flow in a square duct and present results on the detailed structure of the first- and second-order statistics of main and secondary fluid motions, including quantities such as vorticity fluctuations. In particular, we consider a shear or friction Reynolds number of 300 based on duct width for this problem characterized by strong turbulence anisotropy and make direct comparisons with DNS and experimental data of Gavrilakis [9] and Cheesewright *et al.* [34], respectively. We will also present numerical evidence of the size of near-wall quasistreamwise structures arising from wall generated turbulence for this problem as computed in an LBM framework.

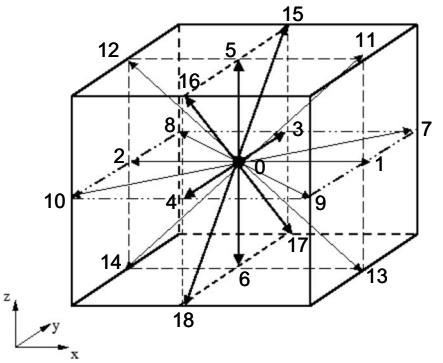

FIG. 1. Schematic illustration of the three-dimensional nineteen velocity (D3Q19) model.

The paper is organized as follows: Section II will discuss the computational procedure that uses GLBE with forcing term. The computational conditions considered for simulation of turbulent flow in a square duct are presented in Sec. III. The computed results and their comparisons with prior data are discussed in Sec. IV. Finally, summary and conclusions of this paper are presented in Sec. V.

II. COMPUTATIONAL PROCEDURE

We shall now discuss the computational procedure based on the generalized lattice Boltzmann equation with a forcing term, which is supplemented by a subgrid scale (SGS) turbulence model. For brevity, we will present only the major elements of the approach, while the details can be found in prior work on MRT [26,28] and in particular those of Yu *et al.* [32], and in the extension for wall-bounded flows subjected to external forces by Premnath *et al.* [33].

A. Generalized lattice Boltzmann equation with forcing term

The lattice Boltzmann method computes the evolution of distribution functions as they move and collide on a lattice grid. The collision process considers their relaxation to their local equilibrium values, and the streaming process describes their movement along the characteristic directions given by a discrete particle velocity space represented by a lattice. Figure 1 represents the three-dimensional nineteen particle velocity (D3Q19) lattice model employed in this paper. The particle velocity $\vec{e}_\alpha$ corresponding to this model may be written as

$$\vec{e}_\alpha = \begin{cases} (0,0,0), & \alpha = 0, \\ (\pm 1,0,0),(0,\pm 1,0),(0,0,\pm 1), & \alpha = 1,\ldots,6, \\ (\pm 1,\pm 1,0),(\pm 1,0,\pm 1),(0,\pm 1,\pm 1), & \alpha = 7,\ldots,18. \end{cases} \quad (1)$$

The GLBE computes collision in moment space, while the streaming process is performed in the usual particle velocity space [26]. The GLBE with forcing term [33] also computes the forcing term, which represents the effect of external forces as a second-order accurate time discretization, in moment space. We use the following notation in our description of the procedure below: In *particle velocity space*, the local distribution function $\mathbf{f}$, its local equilibrium distribution $\mathbf{f}^{eq}$, and the source terms due to external forces $\mathbf{S}$ may be written as the following column vectors: $\mathbf{f}=[f_0,f_1,f_2,\ldots,f_{18}]^\dagger$, $\mathbf{f}^{eq}=[f_0^{eq},f_1^{eq},f_2^{eq},\ldots,f_{18}^{eq}]^\dagger$, and $\mathbf{S}=[S_0,S_1,S_2,\ldots,S_{18}]^\dagger$. Here, the superscript † represents the transpose operator.

The moments $\hat{\mathbf{f}}$ are related to the distribution function $\mathbf{f}$ through the relation $\hat{\mathbf{f}}=\mathcal{T}\mathbf{f}$ where $\mathcal{T}$ is the transformation matrix. Here, and in the following, the "hat" represents the moment space. The transformation matrix $\mathcal{T}$ is constructed such that the collision matrix in moment space $\hat{\Lambda}$ is a diagonal matrix through $\hat{\Lambda}=\mathcal{T}\Lambda\mathcal{T}^{-1}$, where Λ is the collision matrix in particle velocity space. The elements of $\mathcal{T}$ are obtained in a suitable orthogonal basis as combinations of monomials of the Cartesian components of the particle velocity $\vec{e}_\alpha$ through the standard Gram-Schmidt procedure, which are provided by d'Humières *et al.* [26]. Similarly, the equilibrium moments and the source terms in moment space may be obtained through the transformation $\hat{\mathbf{f}}^{eq}=\mathcal{T}\mathbf{f}^{eq}$, $\hat{\mathbf{S}}=\mathcal{T}\mathbf{S}$. The components of moment projections of these quantities are $\hat{\mathbf{f}}=[\hat{f}_0,\hat{f}_1,\hat{f}_2,\ldots,\hat{f}_{18}]^\dagger$, $\hat{\mathbf{f}}^{eq}=[\hat{f}_0^{eq},\hat{f}_1^{eq},\hat{f}_2^{eq},\ldots,\hat{f}_{18}^{eq}]^\dagger$, and $\hat{\mathbf{S}}=[\hat{S}_0,\hat{S}_1,\hat{S}_2,\ldots,\hat{S}_{18}]^\dagger$. These are provided in the Appendix.

The solution of the GLBE with forcing term can be written in terms of the following "effective" collision and streaming steps, respectively:

$$\tilde{\mathbf{f}}(\vec{x},t)=\mathbf{f}(\vec{x},t)+\boldsymbol{\varpi}(\vec{x},t) \tag{2}$$

and

$$f_\alpha(\vec{x}+\vec{e}_\alpha\delta_t,t+\delta_t)=\tilde{f}_\alpha(\vec{x},t), \tag{3}$$

where the distribution function $\mathbf{f}=\{f_\alpha\}_{\alpha=0,1,\ldots,18}$ is updated due to "effective" collision resulting in the postcollision distribution function $\tilde{\mathbf{f}}=\{\tilde{f}_\alpha\}_{\alpha=0,1,\ldots,18}$ before being shifted along the characteristic directions during streaming step. $\boldsymbol{\varpi}$ represents the change in distribution function due to collisions as a relaxation process and external forces, and following Premnath *et al.* [33] it can written as

$$\boldsymbol{\varpi}(\vec{x},t)=\mathcal{T}^{-1}\left[-\hat{\Lambda}(\hat{\mathbf{f}}-\hat{\mathbf{f}}^{eq})_{(\vec{x},t)}+\left(\mathcal{I}-\frac{1}{2}\hat{\Lambda}\right)\hat{\mathbf{S}}_{(\vec{x},t)}\right], \tag{4}$$

where $\mathcal{I}$ is the identity matrix and $\hat{\Lambda}=\mathrm{diag}(s_0,s_1,\ldots,s_{18})$ is the diagonal collision matrix in moment space. It may be noted that some of the relaxation times s_α in the collision matrix, i.e., those corresponding to hydrodynamic modes can be related to the transport coefficients and modulated by eddy viscosity due to the SGS model (discussed below) and the rest chosen to maintain numerical stability [32,33]. Once the distribution function is known, the hydrodynamic fields, i.e., the density ρ, velocity $\vec{u}$, and pressure p can be obtained as follows:

$$\rho=\sum_{\alpha=0}^{18}f_\alpha,\quad \vec{j}\equiv\rho\vec{u}=\sum_{\alpha=0}^{18}f_\alpha\vec{e}_\alpha+\frac{1}{2}\vec{F}\delta_t,\quad p=c_s^2\rho, \tag{5}$$

where $c_s=c/\sqrt{3}$ with $c=\delta_x/\delta_t$ being the particle speed, and δ_x and δ_t are the lattice spacing and time step, respectively. In its implementation, the computational procedure for the solution of the GLBE with forcing term is optimized by fully exploiting the special properties of the transformation matrix $\mathcal{T}$ [32,33].

B. Subgrid scale turbulence model

In this paper, we have incorporated the subgrid scale (SGS) effects in the GLBE through the standard Smagorinsky model to perform LES [15]. The eddy viscosity ν_t arising from this model can be written as

$$\nu_t=(C_s\Delta)^2\bar{S},\quad \bar{S}=\sqrt{2S_{ij}S_{ij}}, \tag{6}$$

where C_s is a constant (taken equal to 0.12 in this work). Here, Δ is the cutoff length scale set equal to the lattice-grid spacing, i.e., $\Delta=\delta_x$, and S_{ij} is the strain rate tensor given by $S_{ij}=1/2(\partial_j u_i+\partial_i u_j)$. In the LBM, the strain rate tensor can be computed directly from the nonequilibrium part of the moments, without the need to apply finite differencing of the velocity field. The specific expressions for the strain rate tensor as a function of nonequilibrium moments and moment projections of source terms are given in the Appendix

To account for the damping of scales near the walls, following an earlier work [35], we have implemented the van Driest damping function [36]

$$\Delta=\delta_x\left[1-\exp\left(-\frac{z^+}{A^+}\right)\right] \tag{7}$$

where $z^+=zu_*/\nu_0$ is the normal distance in wall units from the wall, where u_* is the friction velocity related to the wall shear stress τ_w through $u_*=\sqrt{\tau_w/\rho_0}$, and A^+ is taken equal to 25 [35]. While this approach has some empiricism built in, for a class of wall-bounded turbulent flows, including the turbulent duct flow considered here, it has been shown to be reasonably accurate in prior work based on the solution of grid-filtered Navier-Stokes equations [16]. The eddy viscosity ν_t thus obtained is added to the molecular viscosity ν_0 to obtain the hydrodynamic relaxation times in the collision matrix Λ of the GLBE, as discussed in the previous section.

III. COMPUTATIONAL CONDITIONS

Let us now discuss the details of the computational setup considered in this work. A schematic of the computational domain representing a square duct of width W is shown in Fig. 2. The domain is bounded by four wall boundaries and two open boundaries. The direction along which the main flow with velocity u moves is referred to as the streamwise direction and is represented by the Cartesian coordinate x. The directions parallel to the y and z axes will be designated as spanwise and normal directions, respectively. To facilitate discussion of the results, two normal wall bisectors divide the y-z plane of the duct into four quadrants. The corner wall

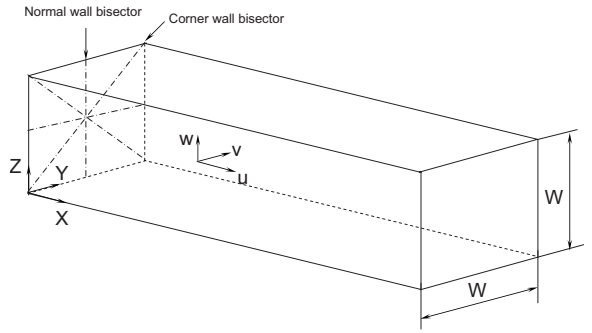

FIG. 2. Schematic of a square duct along with associated coordinate system and nomenclature for turbulence simulation.

bisectors divide each quadrant into areas of equal size.

We consider fully developed turbulent flow of a fluid with nominal density ρ_0 and molecular shear viscosity ν_0, which is driven with a pressure gradient $-dp/dx$, such that the shear Reynolds number $\mathrm{Re}_*=u_*W/\nu_0$ is 300, where u_* is the mean shear or friction velocity. As explained below, in computations we employ periodicity in the streamwise direction and hence the pressure gradient is effectively applied as a simple body force. Here, u_* is related to the wall stress τ_w through $\tau_w=\rho_0 u_*^2$. A simple force balance relates the mean shear velocity to the imposed pressure gradient through $\rho_0 u_*^2=-W(dp/dx)/4$. Zero velocity no-slip wall boundary conditions were applied at each duct wall through a link-based bounce back scheme [37] that places the walls halfway between the lattice grid nodes. The instantaneous flow field is considered to be periodic in the streamwise direction, which is satisfied for the fully developed flow condition considered here and provided that there is spatial decorrelation of turbulence statistics within the domain. The latter condition is satisfied if the streamwise two-point correlation lengths, which represent the characteristic length of the longest streamwise turbulence structures, are properly accommodated by the domain. In DNS, it was found that the correlation length is roughly equal to $3W$ [10]. So, in order for the two-point correlations to decay nearly to zero within half the domain, the required streamwise length of the domain should be about $6W$, which is used in this work.

We considered a uniform grid and the computational domain is discretized by $74\times74\times432$ nodes. The grid spacing in wall units (referred to with a "+" superscript) is taken to be $\Delta^+\equiv\Delta/\delta_\nu=4.16$, where $\delta_\nu=\nu_0/u_*$ is the characteristic viscous length scale. Due to the use of the link-bounce back method for implementation of wall boundary condition, the first lattice node is located at a distance of $\Delta_{nw}^+=\Delta^+/2$, which in our case is 2.08. For wall-bounded turbulent flows, it is important to adequately resolve the near-wall, small-scale turbulent structures, which is satisfied when the computations resolve the local dissipative or Kolmogorov length scale $\eta=(\nu_0^3/\epsilon)^{1/4}$, i.e., $\Delta_{nw}^+\leqslant O(\eta^+)$ [38]. In particular, it is generally recognized that $1.5\eta^+-2.0\eta^+$ represents the upper limit of grid spacing, above which the small scale turbulent motions are not well resolved. It can be shown by simple arguments that $\eta^+=1.5-2.0$ at the wall and that η^+ increases with increasing distance from the wall [39]. Indeed, Madabhushi and Vanka [16] used $\Delta_{nw}^+=2$ in their LES computations of turbulent duct flow using filtered NSE, and our choice of Δ_{nw}^+ is very close to this value. Thus, our computational conditions are expected to fairly resolve the near-wall small-scale turbulent structures.

To perform the GLBE computations corresponding to $\mathrm{Re}_*=300$, we chose the shear viscosity in lattice units ν_0 to be 0.001, and ρ_0 to 1.0, and set up an external driving force $\vec{F}=-\frac{dp}{dx}\hat{x}=\frac{4\rho_0 u_*^2}{W}\hat{x}$. The computations were initially carried out for a period of $10T^*$, where $T^*=W/u_*$ is the nondimensional characteristic time, so that turbulence field reaches a statistically stationary state. They were carried out further for another $6.7T^*$ nondimensional times to obtain turbulence statistics. These sampling times were found to be adequate and in keeping with other prior simulations: Madabhushi and

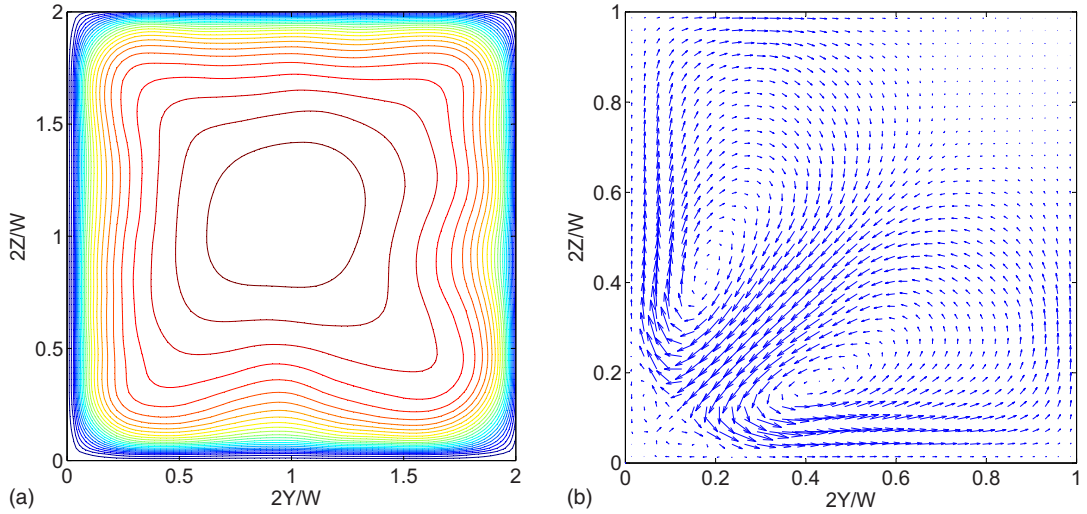

FIG. 3. (Color online) Turbulent flow in a square duct at $\mathrm{Re}_*=300$. (a) Computed contours of the mean streamwise component of the velocity field in the y-z cross section exhibiting corner bulges. (b) Computed mean secondary velocity. Vector field in the y-z cross section in a quadrant of the duct.

TABLE I. Comparison of the coordinate location of the center of the mean vortex (secondary flow) at the lower left corner obtained in different computational studies.

Reference	Center of mean vortex coordinates
DNS (Gavrilakis [9])	$(0.50W, 0.20W)$
DNS (Huser and Biringen [10])	$(0.40W, 0.20W)$
LES–filtered NSE (Madabhushi and Vanka [16])	$(0.55W, 0.25W)$
LES-GLBE (this work)	$(0.45W, 0.18W)$

Vanka [16] used a total duration (for initial run as well as sampling) of $16T^*$ for $\mathrm{Re}_*=360$ LES calculations, while Huser and Biringen [10] used $15T^*$ for the sampling period for DNS at $\mathrm{Re}_*=600$. Gavrilakis [9] used a shorter duration of $3T^*$ for the initial run and $2.5T^*$ for the averaging in his DNS at $\mathrm{Re}_*=300$, as he used considerably longer domain than other studies.

IV. RESULTS AND DISCUSSION

Figure 3(a) shows the computed contours of the mean streamwise velocity in the y-z cross-sectional plane. This figure is obtained by averaging the velocity field over both time and the statistically homogeneous or streamwise direction. A fair degree of symmetry with respect to duct quadrants has been achieved for these contours, similar to that seen in LES based on filtered NSE [16]. The contours of streamwise velocity can be seen to bend towards the walls near to each of the four corners. Prandtl originally explained the distortion of isospeed contours in a square duct to be due to the transport of the faster-moving fluid from the central region toward the corners along the corner bisectors (i.e., low shear region), while slower-moving fluid from the vicinity of the wall is advected toward the center along the duct walls (i.e., high shear region) [2].

Figure 3(b) shows the computed mean cross stream or secondary velocity vector field in the y-z cross sectional plane in a quadrant of the duct. In this figure, and in the following, unless otherwise, statistics of the fluctuating flowfield is obtained by time averaging as well as spatial averaging over the eight similar octants, in addition to the averaging along the streamwise direction. It is evident from this figure that the GLBE is indeed able to predict the existence of secondary flows. It is also consistent with the explanation offered earlier for the bulging of isospeed contours of streamwise velocity field near the four corners of the duct: clearly, two counter-rotating vortices at a duct quadrant appear to transfer fluid momentum from the bulk region of the duct along the corner bisector, which is transported back into the bulk region along the wall bisector. The lower vortex with respect to the corner bisector is centered at about (0.45,0.18), where the numbers in parentheses are the y and z coordinates normalized by the half-width of the duct. This compares well with high-resolution DNS of Gavrilakis [9], which yielded (0.50,0.20). Madabhushi and Vanka [16], in their LES using filtered NSE predicted the center at (0.55,0.25), while Huser and Biringen's [10] DNS (at a higher Reynolds number) gave a value of (0.40,0.20). These results are summarized in Table I. Thus, our computed results are in good general agreement with various prior data.

The presence of turbulence-induced secondary circulations can also be manifested in terms of mean streamwise

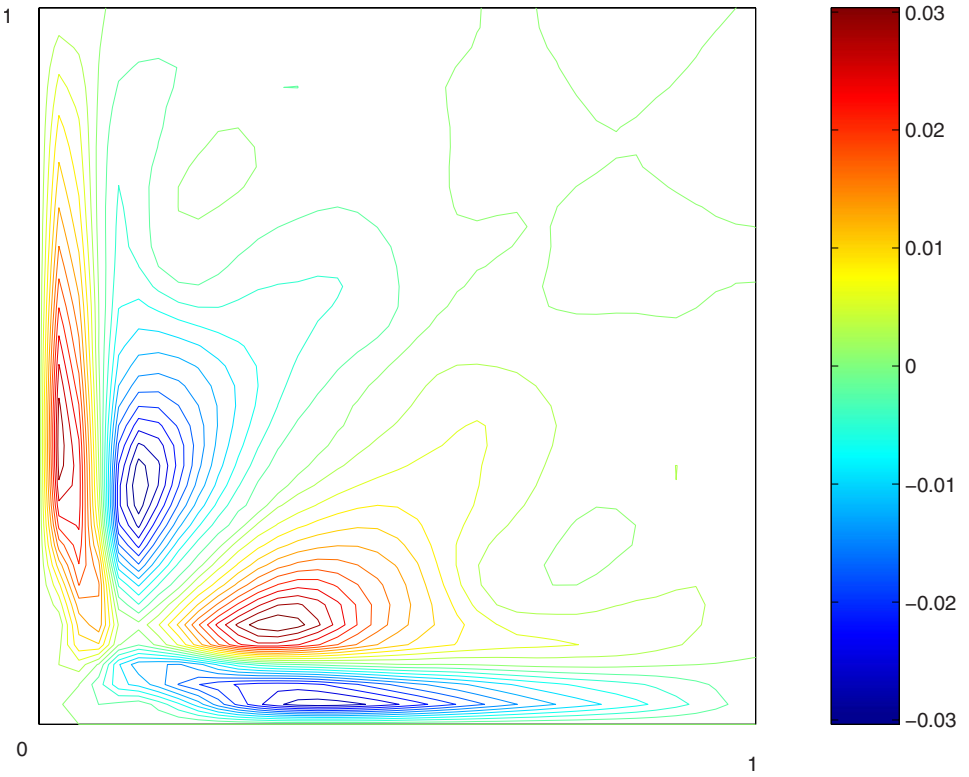

FIG. 4. (Color online) Computed mean streamwise vorticity contours in the lower left quadrant of the duct for turbulent flow in a square duct at $\mathrm{Re}_*=300$.

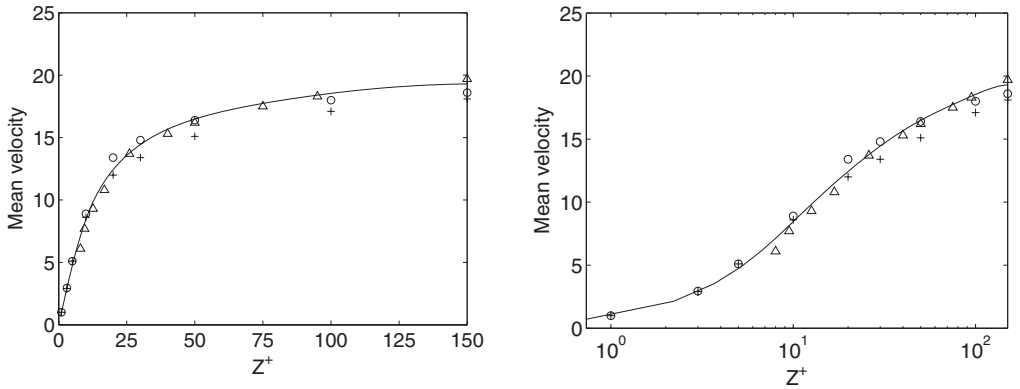

FIG. 5. Mean streamwise velocity profile along wall bisector for turbulent duct flow in a square duct at $\mathrm{Re}_*=300$. Lines represent GLBE prediction, circles and crosses DNS data of Gavrilakis [9] and Huser and Biringen [10], respectively, and triangles LES results based NSE of Madabhushi and Vanka [16].

vorticity contours, which is shown in Fig. 4, where the averaging was performed over a quadrant.

It is clear that streamwise vorticity is generated on either side of the corner bisector, which is consistent with the mean secondary circulations observed in Fig. 3(b). The presence of mean streamwise vorticity owes its origin to a delicate balance between various components of velocity fluctuations or Reynolds stress. In more detail, consider the mean streamwise vorticity equation, which is obtained by eliminating pressure from the mean secondary flow momentum equations and substituting the mean streamwise vorticity [4,40],

$$\langle u_y\rangle\partial_y\langle\omega_x\rangle + \langle u_z\rangle\partial_z\langle\omega_x\rangle = \nu\nabla^2\langle\omega_x\rangle + \partial_y\partial_z(\langle u_y'^2\rangle - \langle u_z'^2\rangle) + (\partial_y\partial_y - \partial_z\partial_z)(\langle -u_y'u_z'\rangle), \quad (8)$$

where $\langle\omega_x\rangle=\partial_y\langle u_z\rangle-\partial_z\langle u_y\rangle$ is the mean streamwise vorticity, with $\langle\cdot\rangle$ being the averaging operator. Note that if the flow is laminar, Reynolds stresses are absent and $\langle\omega_x\rangle=0$, i.e., there will be no mean streamwise vorticity. On the other hand, in turbulent flow, the gradients in the Reynolds stress corresponding to the second and third terms on the right-hand side (RHS) of Eq. (8) act as sources for the production of mean streamwise vorticity. The first term only mediates in the diffusion of vorticity. Now, the second term involves the normal stress anisotropy (i.e., $\langle u_y'^2\rangle\neq\langle u_z'^2\rangle$) and the third term involves a secondary Reynolds stress component ($\langle -u_y'u_z'\rangle$). As can be seen by symmetry considerations, i.e., replacing y with z in the second term on the RHS of Eq. (8), normal Reynolds stress anisotropy is responsible for the generation of mean streamwise vorticity, while the secondary Reynolds stress component sustains secondary flow.

Now, let us discuss various computed turbulence statistics profiles and compare them with prior data. Figure 5 shows the first-order statistics, viz., the mean streamwise velocity profile along the wall bisector, i.e., at $y/W=0.5$.

To be consistent with the data with which the GLBE solution is compared, the velocity is normalized using the *local* shear velocity at the wall bisector, which is computed using the relation $u_\tau^2=\tau/\rho_0$, where τ is the *local* wall stress. This is due to the fact that, unlike the case of turbulent channel flow, turbulent duct flow is characterized by a distribution in wall shear stress. Wall normal distances are normalized by the scale ν_0/u_τ, so that they are provided in terms of the so-called wall units. When compared with DNS of Gavrilakis [9], the mean velocity is slightly overpredicted, as is often the case with LES that use coarser resolutions. On the other hand, the DNS of Huser and Biringen [10] used a lower resolution in the wall-normal direction than Gavrilakis [9] and that is likely to a reason for the higher velocity it predicts, though there could also be Reynolds number effects. Moreover, Huser and Biringen [10] had performed a preliminary DNS at a coarser resolution which had yielded higher velocities than their final DNS solution. The LES of Madabhushi and Vanka [16] also predicted a somewhat higher magnitudes of mean velocity than that of Gavrilakis data, which is consistent with our results. The distribution of the local wall shear stress along the length of one full quadrant is provided in Fig. 6.

The computed local wall stress follows a similar trend to that provided by Gavrilakis [9], with the stress increasing from zero at the corner to a maximum at about a third of the distance to the wall bisector, and then peaking again near the wall bisector. Our results showed somewhat lower values

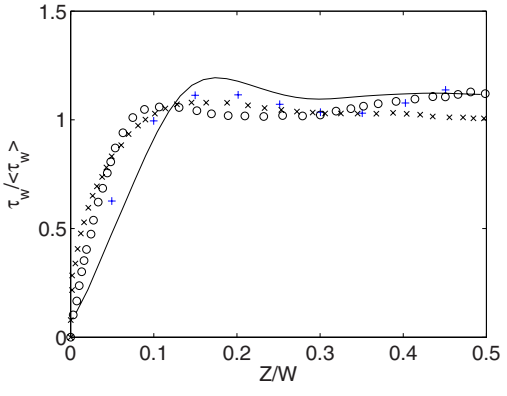

FIG. 6. (Color online) Variation of the local wall stress normalized by the mean wall stress due to turbulent flow in a square duct at $\mathrm{Re}_*=300$. Line represents GLBE prediction, symbols "+" and "○" are DNS data of Gavrilakis [9] and Huser and Biringen [10], respectively, and "×" are LES results based on NSE of Madabhushi and Vanka [16].

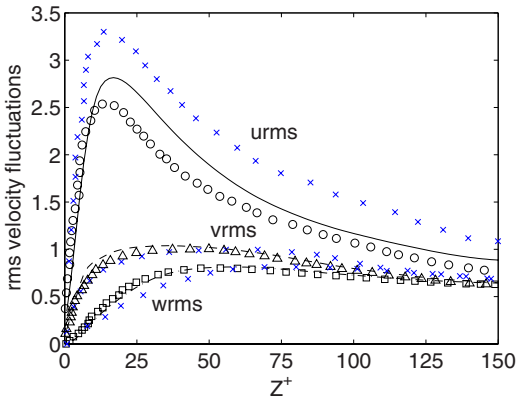

FIG. 7. (Color online) Profile of root-mean-square velocity fluctuations along the wall bisector in the y-z plane for turbulent flow in a square duct at $\mathrm{Re}_*=300$. Lines are GLBE predictions, open symbols DNS data of Gavrilakis [9], and crosses LES results based on NSE of Madabhushi and Vanka [16]. Velocities have been normalized with the shear velocity u_τ.

very close to the corner, which is more likely to be due to the kinetic nature of the boundary conditions of the LBM around the corner, than due to the use of wall damping function. This is because the LES of Madabhushi and Vanka also employed the van Driest wall damping function near walls and their results are closer to the DNS of Huser and Biringen. On the other hand, except for these corner effects, the present results are in overall better agreement with the DNS (Gavrilakis [9]) than that of Madabhushi and Vanka [16]. Figure 7 shows the comparison of computed components of root-mean-square (rms) fluctuations along a wall bisector with prior data.

The level of agreement between the GLBE and the DNS data of Gavrilakis [9] can be seen to be good. In fact, the GLBE predictions show significantly better agreement with the DNS data than the LES results of Madabhushi and Vanka [16], despite the fact that the GLBE computations were carried out with somewhat coarser resolution in the important near-wall region. The significant overprediction of streamwise intensities by Madabhushi and Vanka [16] as compared

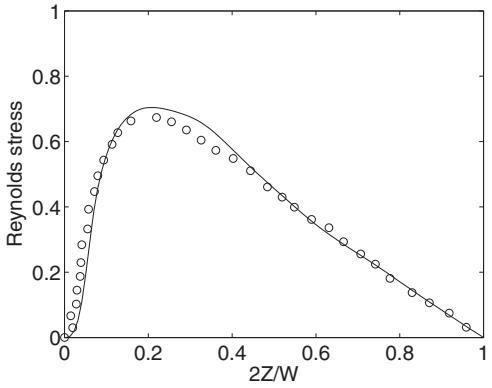

FIG. 8. Profile of mean Reynolds stress along the wall bisector in the y-z plane for turbulent flow in a square duct at $\mathrm{Re}_*=300$. Lines are GLBE predictions and circles are DNS data of Gavrilakis [9].

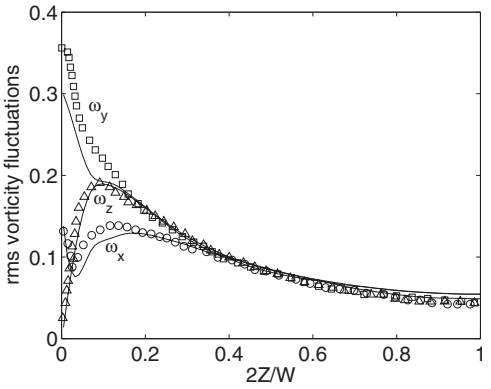

FIG. 9. Profiles of root-mean-square vorticity fluctuations along the wall bisector in the y-z plane for turbulent flow in a square duct at $\mathrm{Re}_*=300$. Lines are GLBE predictions and symbols are DNS data of Gavrilakis [9].

with the DNS is likely to be due to their use of a much coarser resolution than that employed here. The variation of rms turbulence intensities is very similar to that found in other straight wall-bounded flows and comparisons with fully developed turbulent flow in a plane channel data can be found in Gavrilakis [9]. Gavrilakis had raised the question of whether the local shear velocity at the wall center u_τ or the average shear velocity u_* should be used for the normalization of the data. It was found that the agreement with channel flow turbulence intensities was best if u_τ and u_* were used nearer and farther from the wall, respectively.

The distribution of the principal component of Reynolds stress, i.e., $\langle -u_x' u_z' \rangle$ along a wall bisector is shown in Fig. 8.

The variation of Reynolds stress in the duct at this location is very similar to that for a turbulent channel flow, with its maximum occurring at about 1/5th of the duct half-width from the wall. The LES results obtained using the GLBE are in reasonably good agreement with the DNS of Gavrilakis [9].

Accurate representation of near-wall vorticity fluctuations is difficult in LES, as they are very sensitive to the dynamics of small-scale motions generated at the walls, requiring high resolution [41,42]. Figure 9 shows the variation of components of rms vorticity fluctuations along a wall bisector of the duct.

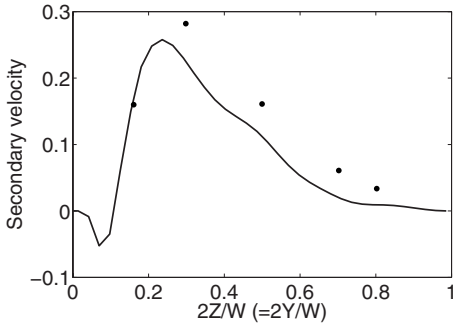

FIG. 10. Magnitude of secondary flows $\langle u_y \rangle \sqrt{2} = \langle u_z \rangle \sqrt{2}$ along a corner bisector for turbulent flow in a square duct at $\mathrm{Re}_*=300$. Circles are DNS data of Gavrilakis [9].

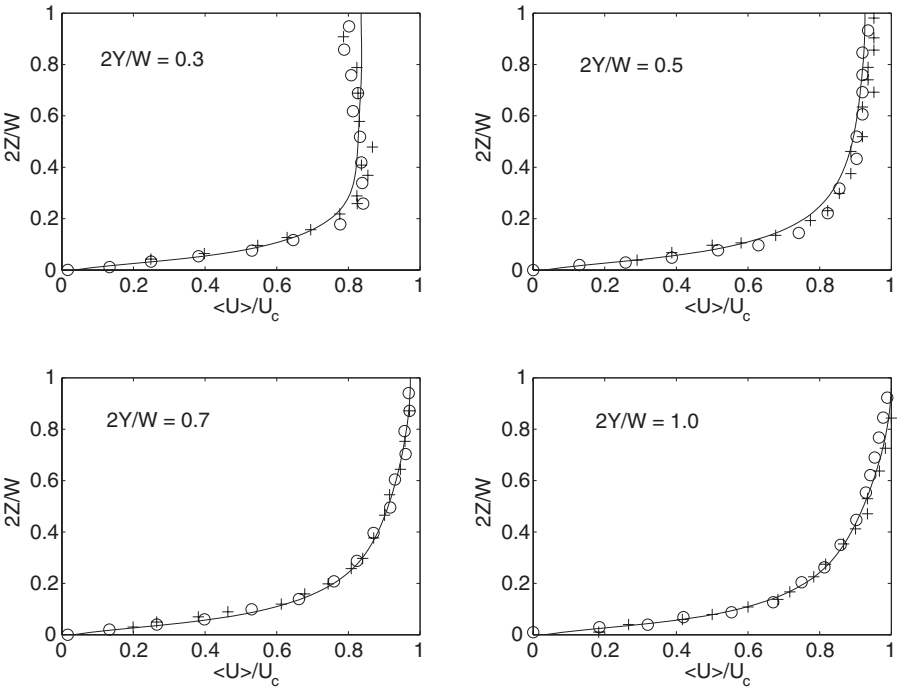

FIG. 11. Profiles of mean streamwise velocities at different locations in the y-z plane in a duct quadrant for turbulent flow in a square duct at $\mathrm{Re}_*=300$. Lines are GLBE predictions, circles are DNS data of Gavrilakis [9], and crosses experimental data of Cheesewright *et al.* [34].

It can be seen from this figure that near-wall turbulent fluctuations are strongly anisotropic and inhomogeneous, while away from the walls they tend to be more isotropic. The GLBE is able to correctly reproduce sharp variations in all the components of rms vorticity fluctuations, when compared with the DNS data of Gavrilakis [9]. Quantitatively, the computed results for the wall-normal vorticity component are in very good agreement, as this component does not involve derivatives of the velocity field with respect to the wall-normal direction. On the other hand, for the other two components, there is some underprediction when compared to finely resolved DNS, a feature very similar to that observed in LES of turbulent channel flow [41,42].

Quantitative prediction of the distribution of the magnitude of secondary flow velocities is challenging partly because of the complex character of its origin, but also because it is relatively small. Figure 10 shows the variation of the magnitude of the secondary velocity along a corner bisector, normalized with the mean shear velocity u_*. The results are compared with those of Gavrilakis and reasonably good agreement can be seen.

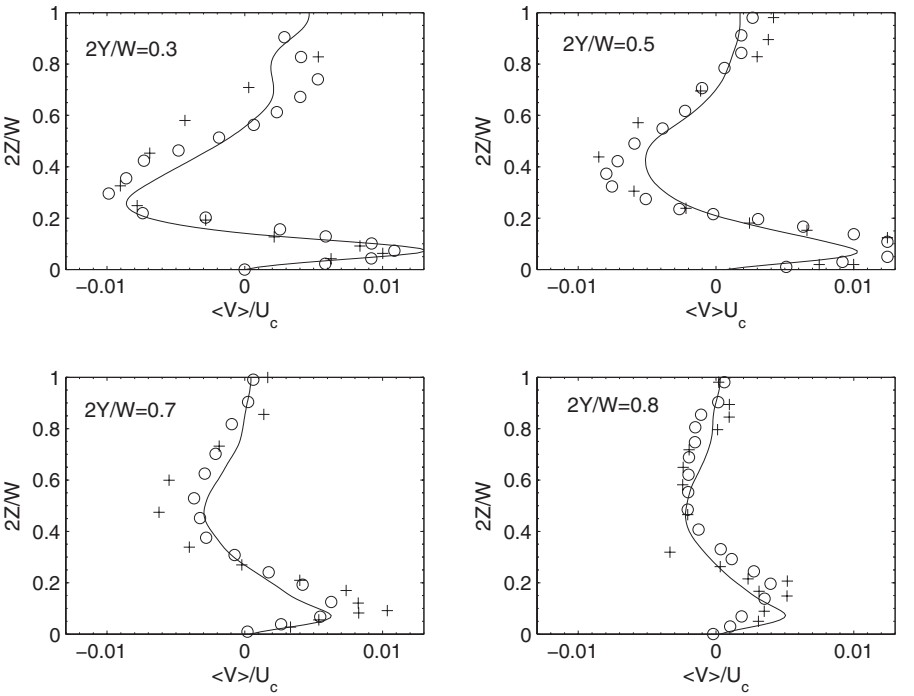

FIG. 12. Profiles of mean secondary velocities at different locations in the y-z plane in a duct quadrant for turbulent flow in a square duct at $\mathrm{Re}_*=300$. Lines are GLBE predictions, circles are DNS data of Gavrilakis [9], and crosses experimental data of Cheesewright *et al.* [34].

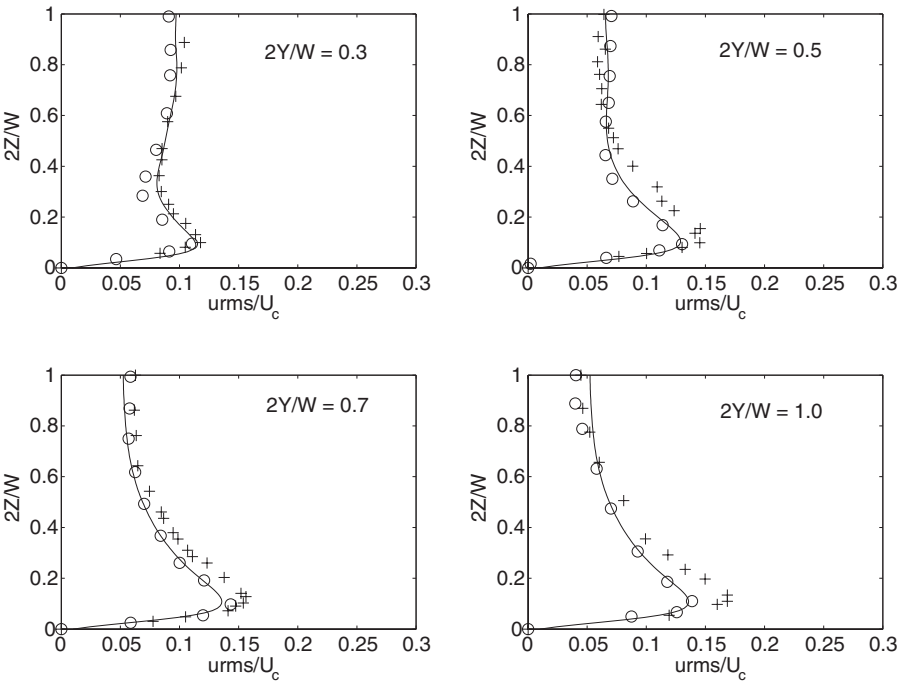

FIG. 13. Profiles of root-mean-square streamwise velocity fluctuations at different locations in the y-z plane in a duct quadrant for turbulent flow in a square duct at $\mathrm{Re}_*=300$. Lines are GLBE predictions, circles are DNS data of Gavrilakis [9], and crosses experimental data of Cheesewright *et al.* [34].

Let us now make quantitative comparisons of the computed detailed structure of the first- and second-order statistics of main and secondary motions at different locations in the duct with high resolution DNS data of Gavrilakis [9] and experimental data of Cheesewright *et al.* [34], which was conducted at a similar, though, slightly lower, Reynolds number. Benchmark data for comparison are available at selected locations in the duct. Figures 11 and 12 present the profiles of mean main (streamwise) and secondary velocities, respectively, at four selected spanwise locations, i.e., $Y/(W/2)=0.3,0.5,0.7,1.0$, in a quadrant of the duct. The velocities are normalized by the mean value of the velocity at the center of the duct U_c. It can be seen that the GLBE predictions are in excellent quantitative agreement with DNS and measurements, not only for the streamwise velocities, but also for the secondary velocities. In particular, the secondary velocities vary quite significantly depending on the location, which the GLBE is able to quantitatively reproduce with very good accuracy. It is also evident from Fig. 12 that the maximum mean secondary velocity is about 1% of the mean streamwise velocity.

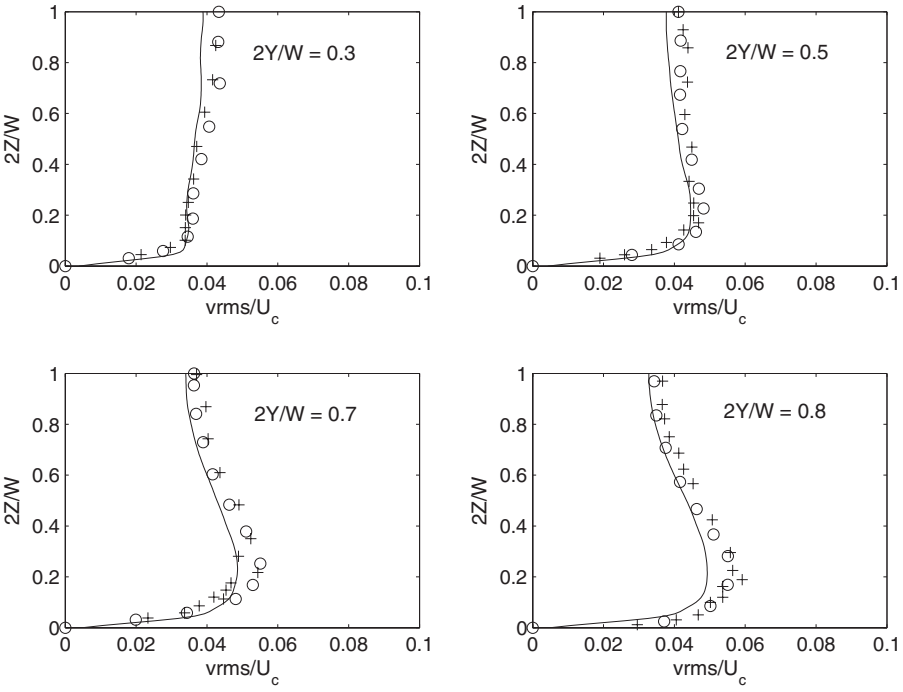

FIG. 14. Profiles of root-mean-square secondary velocity fluctuations at different locations in the y-z plane in a duct quadrant for turbulent flow in a square duct at $\mathrm{Re}_*=300$. Lines are GLBE predictions, circles are DNS data of Gavrilakis [9], and crosses experimental data of Cheesewright *et al.* [34].

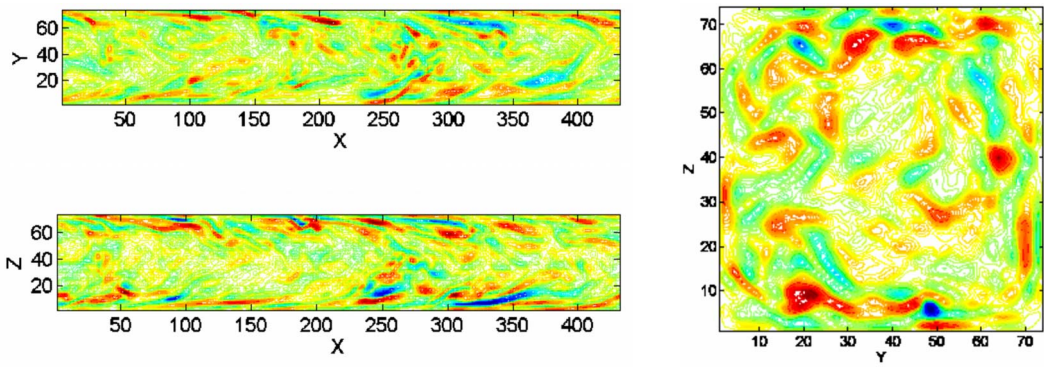

FIG. 15. (Color online) Instantaneous streamwise vorticity in x-y and x-z planes midway between duct walls and in y-z cross section for turbulent flow in a square duct at $\mathrm{Re}_{*}=300$. Flow is from left to right.

Similarly, the second-order statistics of velocity fluctuations, viz., rms main (streamwise) and secondary velocity fluctuations at four selected spanwise locations, i.e., $Y/(W/2)=0.3,0.5,0.7,1.0$ in a quadrant of the duct are shown in Figs. 13 and 14.

It can be seen that the maximum turbulent intensity for the primary flow direction is about 15% of the mean streamwise velocity at the duct center. On the other hand, the maximum turbulent intensity for the cross-stream direction is about one-third that for the primary flow direction. Again, the computed turbulent intensities for both primary and secondary components are in excellent quantitative agreement with both the DNS [9] and measurement data [34].

Our discussions of secondary motions generated due to turbulence have so far been concerned mainly with the averaged quantities. In reality, turbulent flows are far from homogeneous as is illustrated in Fig. 15, which show instantaneous component of the streamwise vorticity at different cross sections.

Wall-bounded flows typically contain quasistreamwise vortices of a few hundred wall units in length [43,44] and such structures are clearly evident in the figures. The lengths of these turbulent structures, as shown in Fig. 15, are about 50 lattice grid spacings, or 200 wall units, which is in keeping with the expected values. These vortices generate sweeps (movements of high speed fluid toward the wall) and ejections (movements of low speed away from the wall) which affect momentum transfer, increasing drag. While the mechanisms responsible for secondary flows are frequently described in terms of Reynolds-averaged Reynolds stresses and vorticities, a more detailed and fundamental explanation necessarily involves discussions of the discrete turbulent structures, such as those based on a quadrant analysis [10].

V. SUMMARY AND CONCLUSIONS

In this work, we performed time-dependent, eddy capturing simulations of turbulent flow and secondary motions in a square duct at shear Reynolds number of 300 using a generalized lattice Boltzmann equation (GLBE) with forcing term. Turbulence-induced mean secondary flows in a square duct results from anisotropy and inhomogeneity in the Reynolds stresses and is challenging to accurately simulate using computational methods. The GLBE is solved in conjunction with a Smagorinsky eddy viscosity model, supplemented with a van Driest damping function, which is used to represent subgrid scale turbulence effects. It was found that the GLBE was able to correctly predict the existence of secondary flows, with its mean motion exhibiting characteristic eightfold symmetry in the form of counter-rotating vortices with respect to corner bisectors of duct quadrants. One of its consequences, i.e., the bulging of isospeed contours of the mean streamwise velocity was also found to be reproduced in computations. Computed profiles of turbulence statistics, including mean streamwise and secondary velocities, Reynolds stress, and root-mean-square turbulent velocity fluctuations and vorticity fluctuations were found to be in good agreement with prior DNS and measurement data. Moreover, the GLBE predictions of detailed structure of the turbulent intensities of both streamwise and secondary velocity components at various locations in the duct are in good quantitative agreement with prior data. Thus, it appears that the GLBE is a reliable and accurate computational method for simulation of complex mean and fluctuations of main and turbulence-induced secondary motions flows due to turbulent flow in a square duct.

ACKNOWLEDGMENTS

This work was performed under the auspices of the National Aeronautics and Space Administration (NASA) under Contract Nos. NNL06AA34P and NNL07AA04C and U.S. Department of Energy (DOE) under Grant No. DE-FG02-03ER83715. Computational resources were provided by the National Center for Supercomputing Applications (NCSA) under Grant No. CTS 060027 and the Office of Science of DOE under Contract No. DE-AC03-76SF00098.

APPENDIX: MOMENTS, EQUILIBRIUM MOMENTS, MOMENT PROJECTIONS OF SOURCE TERMS AND STRAIN RATE TENSOR FOR THE D3Q19 LATTICE

The components of the various elements in the moments are as follows [26]:

$$\hat{f}_0 = \rho, \quad \hat{f}_1 = e, \quad \hat{f}_2 = e^2, \quad \hat{f}_3 = j_x, \quad \hat{f}_4 = q_x, \quad \hat{f}_5 = j_y,$$

$$\hat{f}_6 = q_y, \quad \hat{f}_7 = j_z, \quad \hat{f}_8 = q_z, \quad \hat{f}_9 = 3p_{xx}, \quad \hat{f}_{10} = 3\pi_{xx},$$

$$\hat{f}_{11} = p_{ww}, \quad \hat{f}_{12} = \pi_{ww}, \quad \hat{f}_{13} = p_{xy}, \quad \hat{f}_{14} = p_{yz},$$

$$\hat{f}_{15} = p_{xz}, \quad \hat{f}_{16} = m_x, \quad \hat{f}_{17} = m_y, \quad \hat{f}_{18} = m_z.$$

Here, ρ is the density, e and e^2 represent kinetic energy that is independent of density and square of energy, respectively; j_x, j_y, and j_z are the components of the momentum, i.e., $j_x = \rho u_x$, $j_y = \rho u_y$, $j_z = \rho u_z, q_x, q_y, q_z$ are the components of the energy flux, and p_{xx}, p_{xy}, p_{yz}, and p_{xz} are the components of the symmetric traceless viscous stress tensor; the other two normal components of the viscous stress tensor, p_{yy} and p_{zz}, can be constructed from p_{xx} and p_{ww}, where $p_{ww} = p_{yy} - p_{zz}$. Other moments include π_{xx}, π_{ww}, m_x, m_y and m_z. The first two of these moments have the same symmetry as the diagonal part of the traceless viscous tensor p_{ij}, while the last three vectors are parts of a third rank tensor, with the symmetry of $j_k p_{mn}$.

The corresponding components of the equilibrium moments, which are functions of conserved moments, i.e., density ρ and momentum $\vec{j}$, are as follows [26]:

$$\hat{f}_0^{eq} = \rho, \quad \hat{f}_1^{eq} \equiv e^{eq} = -11\rho + 19\frac{\vec{j}\cdot\vec{j}}{\rho},$$

$$\hat{f}_2^{eq} \equiv e^{2,eq} = 3\rho - \frac{11}{2}\frac{\vec{j}\cdot\vec{j}}{\rho}, \quad \hat{f}_3^{eq} = j_x, \quad \hat{f}_4^{eq} \equiv q_x^{eq} = -\frac{2}{3}j_x,$$

$$\hat{f}_5^{eq} = j_y, \quad \hat{f}_6^{eq} \equiv q_y^{eq} = -\frac{2}{3}j_y, \quad \hat{f}_7^{eq} = j_z,$$

$$\hat{f}_8^{eq} \equiv q_z^{eq} = -\frac{2}{3}j_z, \quad \hat{f}_9^{eq} \equiv 3p_{xx}^{eq} = \frac{[3j_x^2 - \vec{j}\cdot\vec{j}]}{\rho},$$

$$\hat{f}_{10}^{eq} \equiv 3\pi_{xx}^{eq} = 3\left(-\frac{1}{2}p_{xx}^{eq}\right), \quad \hat{f}_{11}^{eq} \equiv p_{ww}^{eq} = \frac{[j_y^2 - j_z^2]}{\rho},$$

$$\hat{f}_{12}^{eq} \equiv \pi_{ww}^{eq} = -\frac{1}{2}p_{ww}^{eq}, \quad \hat{f}_{13}^{eq} \equiv p_{xy}^{eq} = \frac{j_x j_y}{\rho},$$

$$\hat{f}_{14}^{eq} \equiv p_{yz}^{eq} = \frac{j_y j_z}{\rho}, \quad \hat{f}_{15}^{eq} \equiv p_{xz}^{eq} = \frac{j_x j_z}{\rho},$$

$$\hat{f}_{16}^{eq} = 0, \quad \hat{f}_{17}^{eq} = 0, \quad \hat{f}_{18}^{eq} = 0.$$

The components of the source terms in moment space are functions of external force $\vec{F}$ and velocity fields $\vec{u}$, respectively, as follows [33]:

$$\hat{S}_0 = 0, \quad \hat{S}_1 = 38(F_x u_x + F_y u_y + F_z u_z),$$

$$\hat{S}_2 = -11(F_x u_x + F_y u_y + F_z u_z), \quad \hat{S}_3 = F_x, \quad \hat{S}_4 = -\frac{2}{3}F_x,$$

$$\hat{S}_5 = F_y, \quad \hat{S}_6 = -\frac{2}{3}F_y, \quad \hat{S}_7 = F_z, \quad \hat{S}_8 = -\frac{2}{3}F_z,$$

$$\hat{S}_9 = 2(2F_x u_x - F_y u_y - F_z u_z), \quad \hat{S}_{10} = -(2F_x u_x - F_y u_y - F_z u_z),$$

$$\hat{S}_{11} = 2(F_y u_y - F_z u_z), \quad \hat{S}_{12} = -(F_y u_y - F_z u_z),$$

$$\hat{S}_{13} = (F_x u_y + F_y u_x), \quad \hat{S}_{14} = (F_y u_z + F_z u_y),$$

$$\hat{S}_{15} = (F_x u_z + F_z u_x), \quad \hat{S}_{16} = 0, \quad \hat{S}_{17} = 0, \quad \hat{S}_{18} = 0.$$

The components of the strain rate tensor used in subgrid scale (SGS) turbulence models can be written explicitly in terms of nonequilibrium moments augmented by moment projections of source terms as [33]

$$S_{xx} \approx -\frac{1}{38\rho}[s_1\hat{h}_1^{(neq)} + 19s_9\hat{h}_9^{(neq)}], \tag{A1}$$

$$S_{yy} \approx -\frac{1}{76\rho}[2s_1\hat{h}_1^{(neq)} - 19(s_9\hat{h}_9^{(neq)} - 3s_{11}\hat{h}_{11}^{(neq)})], \tag{A2}$$

$$S_{zz} \approx -\frac{1}{76\rho}[2s_1\hat{h}_1^{(neq)} - 19(s_9\hat{h}_9^{(neq)} + 3s_{11}\hat{h}_{11}^{(neq)})], \tag{A3}$$

$$S_{xy} \approx -\frac{3}{2\rho}s_{13}\hat{h}_{13}^{(neq)}, \tag{A4}$$

$$S_{yz} \approx -\frac{3}{2\rho}s_{14}\hat{h}_{14}^{(neq)}, \tag{A5}$$

$$S_{xz} \approx -\frac{3}{2\rho}s_{15}\hat{h}_{15}^{(neq)}, \tag{A6}$$

where

$$\hat{h}_\alpha^{(neq)} = \hat{f}_\alpha - \hat{f}_\alpha^{eq} + \frac{1}{2}\hat{S}_\alpha, \quad \alpha \in \{1,9,11,13,14,15\}. \tag{A7}$$

Here, $\hat{f}_\alpha$, $\hat{f}_\alpha^{eq}$, and $\hat{S}_\alpha$ are components of moments, their local equilibria, and moment projections of source terms due to external forces, respectively, which are given above. s_α are elements of the collision matrix $\Lambda = \mathrm{diag}(s_0, s_1, \ldots, s_{18})$ in moment space. The expressions for the strain rate tensor are generalizations of those given in Yu *et al.* [32].

[1] J. Nikuradse, Ing.-Arch. **1**, 306 (1930).
[2] L. Prandtl, *Essentials of Fluid Dynamics* (Hafner, New York, 1953), p. 148.
[3] H. Schlichting, *Boundary Layer Theory* (McGraw Hill, New York, 1979).
[4] P. Bradshaw, Annu. Rev. Fluid Mech. **19**, 53 (1987).
[5] M. Uhlmann, A. Pinelli, G. Kawahara, and A. Seikmoto, J. Fluid Mech. **588**, 153 (2007).
[6] A. Demuren, AIAA Report No. 90-0245, 1990 (unpublished).
[7] F. Brundrett and W. D. Baines, J. Fluid Mech. **19**, 375 (1964).
[8] F. Gessner, J. Fluid Mech. **58**, 1 (1973).
[9] S. Gavrilakis, J. Fluid Mech. **244**, 101 (1992).
[10] A. Huser and S. Birigen, J. Fluid Mech. **257**, 65 (1993).
[11] A. Demuren and W. Rodi, J. Fluid Mech. **140**, 189 (1984).
[12] C. Speziale, in *Computation of Internal Flows* (ASME, New York, 1984), p. 101.
[13] C. G. Speziale, J. Fluid Mech. **178**, 459 (1987).
[14] S. Nisizima, Theor. Comput. Fluid Dyn. **2**, 61 (1990).
[15] J. Smagorinsky, Mon. Weather Rev. **91**, 99 (1963).
[16] R. K. Madabhushi and S. P. Vanka, Phys. Fluids A **3**, 2734 (1991).
[17] S. Chen and G. Doolen, Annu. Rev. Fluid Mech. **30**, 329 (1998).
[18] S. Succi, *The Lattice Boltzmann Equation for Fluid Dynamics and Beyond* (Clarendon Press, Oxford, 2001).
[19] D. Yu, R. Mei, L.-S. Luo, and W. Shyy, Prog. Astronaut. Aeronaut. **39**, 329 (2003).
[20] R. Nourgaliev, T. Dinh, T. Theofanous, and D. Joseph, Int. J. Multiphase Flow **29**, 117 (2003).
[21] P. Bhatnagar, E. Gross, and M. Krook, Phys. Rev. **94**, 511 (1954).
[22] Y. Qian, D. d'Humières, and P. Lallemand, Europhys. Lett. **17**, 479 (1992).
[23] H. Chen, S. Chen, and W. H. Matthaeus, Phys. Rev. A **45**, R5339 (1992).
[24] D. d'Humières, in *Rarefield Gas Dynamics: Experimental Techniques and Physical Systems*, Progress in Aeronautics and Astronautics, edited by B. D. Shizgal and D. P Weaver (American Institue of Aeronautics & Astronautics, Reston, VA, 1994), p. 450.
[25] P. Lallemand and L.-S. Luo, Phys. Rev. E **61**, 6546 (2000).
[26] D. d'Humières, I. Ginzburg, M. Krafczyk, P. Lallemand, and L.-S. Luo, Philos. Trans. R. Soc. London, Ser. A **360**, 437 (2002).
[27] M. E. McCracken and J. Abraham, Phys. Rev. E **71**, 036701 (2005).
[28] K. N. Premnath and J. Abraham, J. Comput. Phys. **224**, 539 (2007).
[29] K. N. Premnath and J. Abraham, Phys. Fluids **17**, 122105 (2005).
[30] M. J. Pattison, K. N. Premnath, N. B. Morley, and M. Abdou, Fusion Eng. Des. **83**, 557 (2008).
[31] M. Krafczyk, J. Tölke, and L.-S. Luo, Int. J. Mod. Phys. B **17**, 33 (2003).
[32] H. Yu, L.-S. Luo, and S. S. Girimaji, Comput. Fluids **35**, 957 (2006).
[33] K. N. Premnath, M. J. Pattison, and S. Banerjee, preceding paper, Phys. Rev. E **79**, 026703 (2009).
[34] J. Cheesewright, G. McGrath, and D. Petty, Queen Mary Westfield College, University of London, Aeronautical Engineering Department Report No. ER1011, 1990 (unpublished).
[35] P. Moin and J. Kim, J. Fluid Mech. **118**, 341 (1982).
[36] E. van Driest, J. Aeronaut. Sci. **23**, 1007 (1956).
[37] A. Ladd, J. Fluid Mech. **271**, 285 (1994).
[38] K. Moin and K. Mahesh, Annu. Rev. Fluid Mech. **30**, 539 (1998).
[39] S. Pope, *Turbulent Flows* (Cambridge University Press, New York, 2000).
[40] H. Perkins, J. Fluid Mech. **44**, 721 (1970).
[41] T. Lê and V. Maupu, *Engineering Turbulence Modeling and Experiments 2*, edited by W. Rodi and L. Martelli (Elsevier Science, Amsterdam, 1993), p. 335.
[42] Y. Dubief and F. Delcayre, J. Turbul. **1**, 1 (2000).
[43] S. Banerjee, Chem. Eng. Sci. **47**, 1793 (1992).
[44] C. Marchioli, M. Picciotto, and A. Soldati, *Modelling and Experimentation in Two-Phase Flow* (Springer Verlag, Berlin, 2004), p. 119.